Post-Test Inspection of NASA's Evolutionary Xenon Thruster Long Duration Test Hardware: Ion Optics

George C. Soulas and Rohit Shastry
Glenn Research Center, Cleveland, Ohio

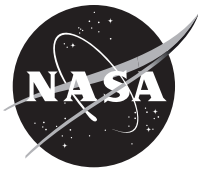# NASA STI Program . . . in Profile

Since its founding, NASA has been dedicated to the advancement of aeronautics and space science. The NASA Scientific and Technical Information (STI) Program plays a key part in helping NASA maintain this important role.

The NASA STI Program operates under the auspices of the Agency Chief Information Officer. It collects, organizes, provides for archiving, and disseminates NASA's STI. The NASA STI Program provides access to the NASA Technical Report Server—Registered (NTRS Reg) and NASA Technical Report Server— Public (NTRS) thus providing one of the largest collections of aeronautical and space science STI in the world. Results are published in both non-NASA channels and by NASA in the NASA STI Report Series, which includes the following report types:

- TECHNICAL PUBLICATION. Reports of completed research or a major significant phase of research that present the results of NASA programs and include extensive data or theoretical analysis. Includes compilations of significant scientific and technical data and information deemed to be of continuing reference value. NASA counter-part of peer-reviewed formal professional papers, but has less stringent limitations on manuscript length and extent of graphic presentations.

- TECHNICAL MEMORANDUM. Scientific and technical findings that are preliminary or of specialized interest, e.g., "quick-release" reports, working papers, and bibliographies that contain minimal annotation. Does not contain extensive analysis.

- CONTRACTOR REPORT. Scientific and technical findings by NASA-sponsored contractors and grantees.

- CONFERENCE PUBLICATION. Collected papers from scientific and technical conferences, symposia, seminars, or other meetings sponsored or co-sponsored by NASA.

- SPECIAL PUBLICATION. Scientific, technical, or historical information from NASA programs, projects, and missions, often concerned with subjects having substantial public interest.

- TECHNICAL TRANSLATION. English-language translations of foreign scientific and technical material pertinent to NASA's mission.

For more information about the NASA STI program, see the following:

- Access the NASA STI program home page at http://www.sti.nasa.gov

- E-mail your question to help@sti.nasa.gov

- Fax your question to the NASA STI Information Desk at 757-864-6500

- Telephone the NASA STI Information Desk at 757-864-9658

- Write to:
  NASA STI Program
  Mail Stop 148
  NASA Langley Research Center
  Hampton, VA 23681-2199

Post-Test Inspection of NASA's Evolutionary Xenon Thruster Long Duration Test Hardware: Ion Optics

George C. Soulas and Rohit Shastry
Glenn Research Center, Cleveland, Ohio

National Aeronautics and
Space Administration

Glenn Research Center
Cleveland, Ohio 44135

June 2021

Acknowledgments

Level of Review: This material has been technically reviewed by technical management.

Available from

Post-Test Inspection of NASA's Evolutionary Xenon Thruster Long Duration Test Hardware: Ion Optics

George C. Soulas and Rohit Shastry
National Aeronautics and Space Administration
Glenn Research Center
Cleveland, Ohio 44135

Abstract

A Long Duration Test (LDT) was initiated in June 2005 as a part of NASA's Evolutionary Xenon Thruster (NEXT) service life validation approach. Testing was voluntarily terminated in February 2014, with the thruster accumulating 51,184 hours of operation, processing 918 kg of xenon propellant, and delivering 35.5 MN-s of total impulse. The post-test inspection objectives for the ion optics were derived from the original NEXT LDT test objectives, such as service life model validation, and expanded to encompass other goals that included verification of in situ measurements, test issue root causes, and past design changes. The ion optics cold grid gap had decreased only by an average of 7 percent of pretest center grid gap, so efforts to stabilize NEXT grid gap were largely successful. The upstream screen grid surface exhibited a chamfered erosion pattern. Screen grid thicknesses were ≥ 86 percent of the estimated pretest thickness, indicating that the screen grid has substantial service life remaining. Deposition was found on the screen aperture walls and downstream surfaces that was primarily composed of grid material and back-sputtered carbon, and this deposition likely caused the minor decreases in screen grid ion transparency during the test. Groove depths had eroded through up to 35 percent of the accelerator grid thickness. Minimum accelerator aperture diameters increased only by about 5 to 7 percent of the pretest values and downstream surface diameters increased by about 24 to 33 percent of the pretest diameters. These results suggest that increasing the accelerator aperture diameters, improving manufacturing tolerances, and masking down the perforated diameter to 36 cm were successful in reducing the degree of accelerator aperture erosion at larger radii.

Nomenclature

ELT   (NSTAR) Extended Life Test
GRC   NASA Glenn Research Center
ID   Inner diameter surface relative to the ion optic's center
LDT   (NEXT) Long Duration Test
NEXT   NASA's Evolutionary Xenon Thruster
NEXT-C   NASA's Evolutionary Xenon Thruster-Commercial
NSTAR   NASA's Solar Electric Propulsion Technology Applications Readiness
OD   Outer diameter surface relative to the ion optic's center
PM   Prototype Model

1.0 Introduction

The NASA Glenn Research Center (GRC) is responsible for the development of NASA's Evolutionary Xenon Thruster (NEXT) ion propulsion system (Ref. 1). The NEXT system is a next generation ion propulsion system to follow the successful NASA's Solar Electric Propulsion Technology

Applications Readiness Program (NSTAR) ion propulsion system that propelled NASA's Deep Space 1 spacecraft and is presently propelling the Dawn spacecraft (Refs. 2 and 3). Propulsion system elements developed by the NEXT project include a high performance, 7 kW ion thruster; a high-efficiency 7 kW power processor unit; a highly flexible advanced xenon propellant management system; and a compact, light-weight thruster gimbal. In 2015, the NEXT project transitioned from development to providing spaceflight hardware under the new project name NASA's Evolutionary Xenon Thruster-Commercial (NEXT-C). The flight hardware for the NEXT-C project includes two thrusters and two power processor units and is being manufactured by Aerojet Rocketdyne, Inc. for use on NASA missions.

The NEXT ion thruster service life capability is being assessed through a service life validation approach that utilizes a combination of testing and analyses (Refs. 4 to 8). The NEXT thruster, as a second-generation deep-space ion thruster, has made use of over 70,000 hours of ground and flight test experience (not including the accumulated hours from the NSTAR ion thrusters on the ongoing Dawn mission) in both the design of the NEXT thruster and the evaluation of thruster wear-out failure modes. A service life assessment was conducted at NASA GRC, employing several models to evaluate all known failure modes that were based upon the substantial amount of ion thruster testing dating back to the early 1960s (Refs. 4 and 5). The service life assessment also incorporated results from the NEXT 2000 h wear test conducted on a laboratory model thruster operating at full power (i.e., 6.9 kW) (Ref. 6).

The NEXT Long Duration Test (LDT) was initiated in June 2005 to validate the NEXT thruster service life model as well as quantify the NEXT thruster lifetime. Descriptions of the test setup and vacuum facility can be found in Reference 8 and the references cited therein. The goals of the NEXT LDT were to demonstrate the initial project qualification propellant throughput requirement of 450 kg, validate thruster service life model's predictions, quantify thruster performance and erosion as a function of thruster wear and throttle level, and identify any unknown life-limiting mechanisms. In December 2009, after successfully demonstrating the original qualification throughput requirement of 450 kg, the first listed goal was redefined to voluntary test termination.

The thruster was successfully operated to February 2014. At the time of voluntary test termination, the thruster had accumulated 51,184 hours of high-voltage operation, processed 918 kg of propellant, and delivered 35.5 MN-s of total impulse. The NEXT thruster has demonstrated a significant improvement in thruster lifetime compared to the existing state-of-the-art NSTAR thruster, and has set numerous records for the most demonstrated lifetime of an electric propulsion device. Just prior to voluntary test termination, the thruster was retracted into its independently-pumped port and isolated from the main vacuum facility so that diagnostics that had failed during the test could be repaired (Ref. 8). A thruster performance test was conducted with the repaired diagnostics to fully characterize the end-of-test performance and condition of the thruster. In April 2014, the thruster was exposed to atmosphere for the first time in nearly nine years. After in situ photographs and measurements were made, the thruster was moved to a clean room for post-test inspection.

The post-test inspection of the LDT ion thruster includes examinations of all major assemblies. These assemblies include the ion optics, discharge chamber, and the cathode assemblies of the discharge chamber and neutralizer. This paper will present the post-test inspection results to date for the LDT thruster's ion optics assembly. Post-test inspection results for the discharge chamber and cathode assemblies are presented in companion papers (Refs. 9 and 10). The next section describes the post-test inspection objectives. Afterwards, the LDT thruster and ion optics assembly are described. The sections thereafter describe the post-test inspection results to date for the ion optics. Finally, a summary of the results is presented.

2.0   Post-Test Inspection Objectives and Plan

The post-test inspection objectives were derived from the original LDT test objectives and expanded to encompass other goals. A primary objective of post-test inspection is to measure the wear rates of critical surfaces and use these results to verify and update service life models. With regards to the ion optics, these eroded critical surfaces are those associated with the NEXT ion thruster credible failure modes of Reference 4 and include the downstream accelerator grid surfaces, accelerator aperture walls, and the upstream screen grid surfaces. Charge exchange ions will erode a hexagonally-shaped trench along the downstream webbing of an accelerator aperture with pits at the six corners of the hexagon connected by grooves. Accelerator grid structural failure occurs when the pits and grooves all erode through the grid thickness, and this hexagonally shaped section can either bridge the gap between the grids and create an electrical short or, if removed, the resulting hole will lead to electron backstreaming. This failure mode was modeled to be the first throughout the NEXT throttle table (Refs. 4 and 5). Charge-exchange ions will also erode accelerator aperture walls, enlarging their open area. If this area exceeds the ability of the accelerator voltage to prevent neutralizer electrons from backstreaming through the ion optics, the ion optics will be unable to produce the required thrust. Finally, discharge chamber ions will erode the screen grid's upstream surface, which reduces its thickness. If screen webbing is eroded away, ions will no longer be focused through the accelerator apertures and will erode the upstream accelerator grid webbing. This will potentially accelerate other optics failure modes or the increased accelerator current could be too large for the power processor unit's accelerator power supply.

A fourth failure mode associated with the ions optics is an unclearable electrical short by conductive debris bridging the gap between the grids (Ref. 4). An electrical short between the grids would prevent application of high voltage, thus inhibiting the acceleration of ions and would result in an inability to produce thrust. The NEXT power processor is, however, equipped with a grid clear circuit that can deliver up to 24 A through the electrical short to ablate the debris. The sources of this debris include the external launch environment and spalled flakes from the discharge chamber, but also include spalled flakes from sputter-deposited films on the grids. Therefore, a goal of post-test inspection is to evaluate the deposition on the grids.

The NEXT LDT was equipped with a number of imaging diagnostics that were used to map the temporal behavior of thruster erosion (Ref. 8). For the ion optics, these diagnostics included cameras that imaged apertures at the grid center, a radius of 16.3 cm, and the apertures at the edge of the perforated grid; a camera that measured the cold grid gap at the optics center; and, later in the test, the cameras at the center aperture were adapted to measure groove depth (Ref. 11). So, a goal of post-test inspection is to verify in situ measurements with post-test measurements.

During the nine year LDT, a number of thruster-related issues and concerns were identified. Although causes were determined in most cases, post-test inspections are necessary for verification. Those related to the ion optics included ion optics high voltage impedance degradations, unanticipated ion optics performance trends, sources of rogue holes (i.e., anomalously enlarged accelerator apertures), and differences between erosion models and observed erosion. So, post-test inspections will investigate those areas of concern to better understand and verify root causes.

The NEXT LDT incorporate changes that were derived from an earlier 2000 h wear test (Ref. 6). Those associated with the ion optics included a change in compensation for better aperture alignment between the grids, and masking down the perforated diameter from 40 to 36 cm and increased accelerator aperture diameters with improved manufacturing tolerances to reduce beamlet over-focusing accelerator aperture erosion at lower beamlet currents. So, a goal of post-test inspections is to verify that these changes made to the NEXT LDT ion optics had the desired impacts.

Finally, as with any extended testing, an objective of post-test inspections is to identify any unanticipated thruster life-limiting phenomena.

3.0 Thruster and Ion Optics Description

The NEXT LDT is a modified version of a NEXT thruster (designated EM3) and is shown in Figure 1. The NEXT thruster is nominally a 0.5 to 6.9 kW input power xenon thruster, capable of producing thrust values from 25 to 235 mN and specific impulses from 1400 to 4160 sec (Ref. 12). The technical approach for the NEXT design continues the derating philosophy used for the NSTAR ion thruster. A beam extraction area 1.6 times that of the NSTAR thruster allows for operation at higher thruster input powers while maintaining low voltages and ion current densities, thus maintaining thruster service life. A semi-conic discharge chamber utilizes a hollow cathode emitter with a ring-cusp magnetic field topology created by high strength, rare earth magnets for electron confinement. A graphite discharge cathode keeper electrode was also incorporated into the thruster for improved service life. A flake retention scheme, identical to that employed on the NSTAR thruster, enhances the adhesion of thin films to the discharge chamber surfaces (Ref. 13). New, compact propellant isolators with higher voltage isolation capability than those used by the NSTAR thruster are also utilized (Ref. 14). The NEXT neutralizer design is mechanically similar to the International Space Station Plasma Contactor Hollow Cathode Assembly, leveraging this extensive database to further reduce risk (Refs. 15 and 16).

The NEXT thruster's ion optics utilizes a convex, two grid system. To obtain a flight-representative configuration, prototype model (PM) ion optics were incorporated and were provided by Aerojet (now Aerojet Rocketdyne) (Ref. 17). Changes were made with the PM ion optics design to address issues and risks that had been identified early in the project (Refs. 6 and 17). The PM ion optics beam extraction diameter was reduced to 36 cm diameter to reduce outer-radius accelerator aperture erosion caused by beamlet over-focusing in these low current density regions. Reducing the ion optics beam extraction diameter from the original 40 cm diameter also reduces the maximum thruster beam divergence and neutral loss rate without significant increases in discharge losses. The PM ion optics geometry retains many of the key features of the past NASA design; however, improved manufacturing techniques led to better control of aperture diametric tolerances across the grid and a reduced cusp profile from the etching process used to manufacture the apertures. Also, the PM ion optics mounting scheme was altered to

Figure 1.—Pretest image of the NEXT LDT thruster.

eliminate the buildup and relaxation of assembly- and thermally-induced stresses that can lead to the decreasing ion optics grid-gap with test duration (Refs. 6, 18, and 19).

Throughout this publication, comparisons will be made to the life tested ion optics of the NSTAR thruster because of similarities between the designs (Refs. 18 to 21). The screen grid apertures diameters, center-to-center aperture spacing, and thicknesses are similar between the two designs. However, the NEXT LDT thruster cold grid gap at the grid center was 7.7 percent larger than that of the nominal NSTAR gap. In addition, the NEXT accelerator grid was 50 percent thicker for improved service life capability and the aperture diameters for the LDT optics were about 11 percent larger than the nominal NSTAR design diameter.

4.0   Ion Optics Post-Test Inspection Results

The following sections present the post-test inspection results for the ion optics. The first section describes the post-test condition of the ion optics assembly. The sections thereafter describe the screen and accelerator grid post-test inspection results to date.

4.1   Ion Optics Assembly Post-Test Condition

The following sections present the overall condition of the ion optics assembly and measurements of high voltage impedances, fastener integrity, ion optics assembly mass, and cold grid gap.

4.1.1   Overall Ion Optics Condition

An image of the post-test ion optics mounted on the NEXT LDT thruster is given in Figure 2. The dark areas of the exposed accelerator grid are net deposits of back-sputtered carbon from the graphite panels lining the interior of the vacuum facility. These dark areas of net carbon deposition are persistent throughout most of the perforated area of the grid, including the grid central area. This is discussed in greater detail in the accelerator grid section and the Appendix. A photograph of the upstream screen grid is shown in Figure 3. Most of the exposed grid surface appears metallic with some uneven discoloration along the outer perimeter of the unperforated region of the grid. More detailed screen and accelerator grid inspection results will be shown in later sections.
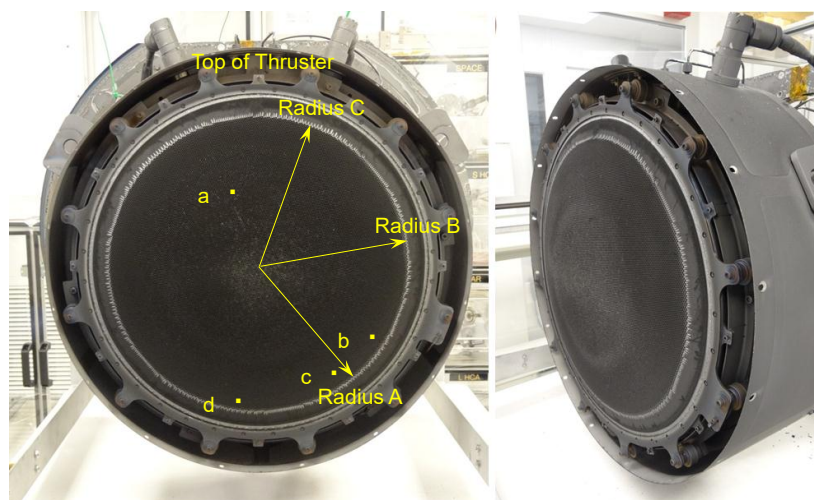

Figure 2.—Post-test ion optics assembly mounted on the NEXT LDT thruster but with the front mask and neutralizer removed. The three radii for the measurements and images presented herein are also shown. The yellow squares labeled a to d identify approximate locations of rogue holes.

Figure 3.—Post-test upstream screen grid mounted to the ion optics assembly. The orientation of the neutralizer is shown.

4.1.2 High Voltage Impedance Measurements and Fastener Preloads

During the NEXT LDT, the impedance between the grids had decreased and exhibited a polarity-dependent behavior when measured with an applied high voltage. Though this was not a problem, there was interest in determining if this behavior was facility-induced (e.g., a carbon flake between the grids). Following thruster exposure to atmosphere, a low impedance path between the screen and accelerator grids was measureable with an ohmmeter. Unfortunately, this low impedance path was lost following removal of the ion optics assembly from the thruster, so the source could not be identified. Inspection of the disassembled ion optics further yielded no obvious sources of a low impedance path.

Following removal of the accelerator grid subassembly, the impedances of the 12 insulators that attach the accelerator grid subassembly to its mounting ring were individually measured with an applied voltage of 2025 V. All were found to have an impedance of $> 2.04 \times 10^{12}$ Ω (i.e., beyond the upper limit of the measuring device), indicating that the insulators had not degraded with operation.

All ion optics assembly threaded fastener breakaway torques were measured during disassembly. The lowest breakaway torque was 85 percent of the minimum applied torque requirement, indicating that all fasteners were still preloaded.

4.1.3 Mass Changes

The masses of the ion optics assembly and its subassemblies were measured both pre- and post-test. The ion optics assembly mass was found to have decreased by 30.3 gm. The accelerator grid subassembly mass was measured to have decreased by 29.5 gm. The screen grid subassembly was independently measured and found to have decreased by only 0.8 gm. Although the latter two measurements were made at the subassembly level and therefore include components used to secure the electrodes to the mounting system, they likely reflect electrode mass losses because the electrodes are the only parts exposed to any eroding plasma or to significant deposition.

The NEXT LDT accelerator and screen grid mass losses are less than the 33.7 and 3.2 gm, respectively, lost from the NSTAR grids during the 30.4 kh Extended Life Test (ELT) (Ref. 19). Although the NEXT LDT thruster operates at twice the NSTAR beam current at full power, there are a number of reasons for the reduced NEXT LDT mass losses and these will be discussed in the subsequent sections for each grid.

4.1.4 Cold Grid Gap

The cold grid gap (i.e., the grid gap with the screen and accelerator grids at room temperature) was measured pre- and post-test along the three radii illustrated in Figure 2 with gapping gages. The differences between pre- and post-test measurements are shown in Figure 4 as a percentage of the pretest grid gap at the ion optics center. The measurement uncertainty was estimated to be ±4 percent of pretest grid gap at the grid center. The measurements were corrected by excluding the screen grid downstream surface deposition, which was 2.8 to 5.3 percent of the center cold grid gap and will be discussed in the screen grid section. The graph shows that the grid gap had decreased and that these decreases were typically 2 to 13 percent of pretest center grid gap. The average of all measurements was a decrease of 7 percent of pretest center grid gap. This decrease is substantially less than the 30 percent decrease measured for the NSTAR thruster following the ELT (Ref. 19). These results show that efforts to stabilize NEXT ion optics grid gap were largely successful.

The cold grid gap at the center of the ion optics was measured in situ throughout the NEXT LDT and was found to have remained unchanged (Ref. 8). However, post-test measurements show that the grid gap at the optics center had decreased by 4 percent of the pretest value, as shown in Figure 4. The primary reason for this discrepancy was that the uncertainties of both measurement techniques overlapped. The post-test measurement uncertainty was ±4 percent and in situ uncertainty was ±6.4 percent of the pretest gap. So the change in grid gap at the optics center was ultimately too small to discern.

4.2 Screen Grid

Post-test inspections of the screen grid included both nondestructive and destructive inspection methods. Nondestructive inspection methods included photomicrographs of upstream and downstream aperture surfaces, upstream surface profiles of several apertures with a profilometer, and aperture diameter measurements with pin gages. Destructive inspection included laser cutting the grid into smaller
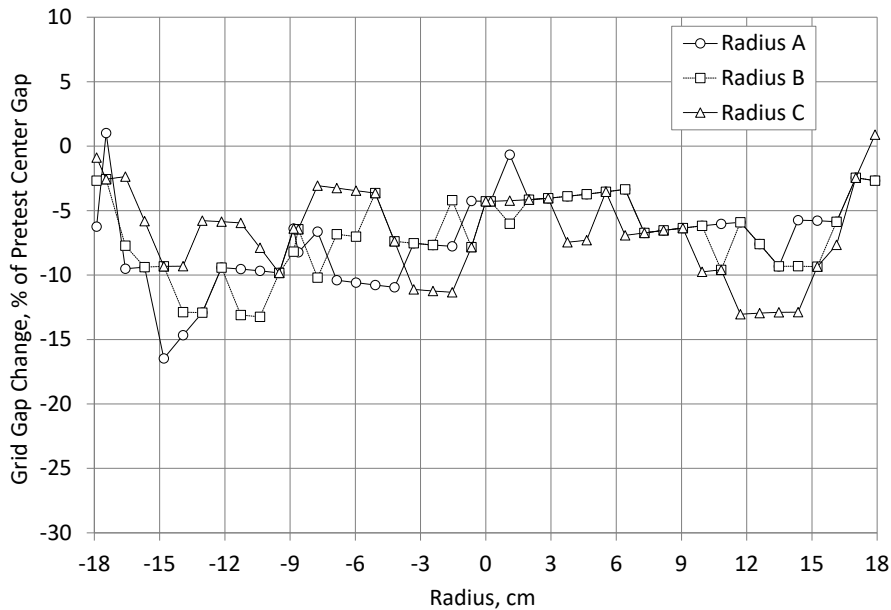

Figure 4.—Cold grid gap change as a function of radius along three radii (see Figure 2 for radial orientations). The post-test measurement excludes deposition. The grid gap is expressed as a percentage of the pretest grid gap at the ion optics center. The measurement uncertainty was estimated to be ±4 percent.

sections so that aperture webbing cross sections could be inspected with optical and scanning electron microscopes. Compositions were determined with energy dispersive x-ray spectroscopy. The following sections will present the results of those inspections. The first section will discuss upstream surface erosion and its impact on service life. The second section will present the deposition on the aperture walls and upstream surface. The third section will discuss the change in aperture diameter and its impact on thruster performance. Finally, the change in screen grid mass will be evaluated.

4.2.1   Upstream Surface Erosion

Post-test images of the screen grid upstream surfaces are shown in Figure 5 at various radial locations. The upstream screen surface exhibited a chamfered erosion pattern that was pronounced near the center of the grid and faded away at larger radii. This erosion pattern is very similar to that of the NSTAR thruster that was measured following the ELT (Ref. 19). Surface profilometry of this chamfering at several radial locations is shown in Figure 6. The images show six peaks separated by connecting ridges of decreased height to form the chamfered appearance. Of the several profiles measured, the difference in heights between the peaks and ridges was measured to be within about 5.2 percent of the nominal grid thickness. Ridges perpendicular to the radial direction of the optics increased in height with optics radius until they were level with the adjacent peaks.

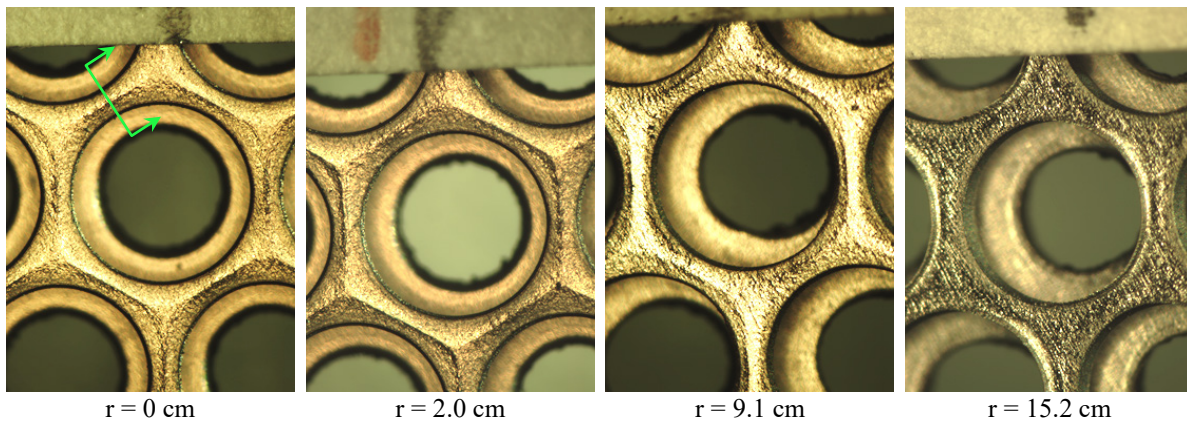| r = 0 cm | r = 2.0 cm | r = 9.1 cm | r = 15.2 cm |

Figure 5.—Post-test images of upstream screen grid surfaces at various radial locations along radius C (see Figure 2). All images are oriented with the grid center to the left and the outer perimeter to the right. For all images, the camera was pointing in the axial direction; so the screen and corresponding accelerator apertures appear misaligned because of the grids' curvature. The green arrows of the r = 0 cm image indicate the orientation of screen grid sectioning.
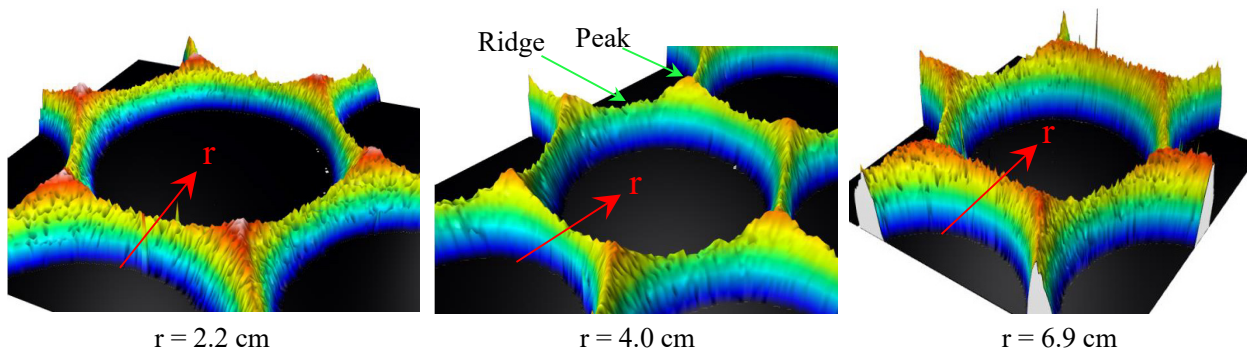

| r = 2.2 cm | r = 4.0 cm | r = 6.9 cm |

Figure 6.—Post-test profiles of upstream screen grid surfaces at various radial locations along radius C (see Figure 2). The arrows indicate increasing radius from the optics center. The eroded depth was exaggerated for clarity. A ridge and peak are indicated in the r = 4.0 cm profile.

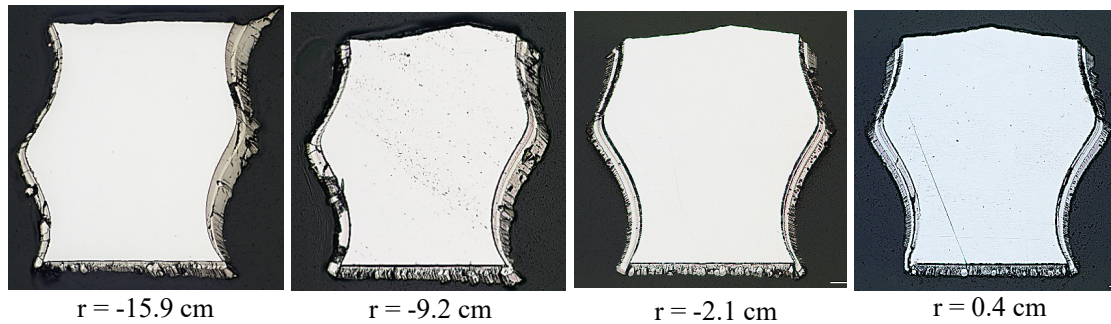| r = -15.9 cm | r = -9.2 cm | r = -2.1 cm | r = 0.4 cm |

Figure 7.—Photomicrographs of screen grid webbing cross sections at various radial locations along radius B (see Figure 2). Figure 5 shows the orientation of the grid sectioning. All images are oriented with the optics center to the right and the outer perimeter to the left; the top surfaces are the upstream surfaces. The white central region is the grid webbing substrate and the grayish material surrounding the webbing is deposition.

Because the worst case screen webbing erosion was closer to the center of a ridge, the screen grid wedding was sectioned at the middle of a screen web for inspection as shown in Figure 5. The grid sections were mounted in epoxy prior to polishing to ensure that grid deposition was not removed during the preparation process. Sample screen grid webbing cross sections are shown in Figure 7 at various radial locations. The grid was sectioned along radius B of Figure 2 because this radius most closely tracked beam current density measurements. In addition, most measurements were made along the negative radius side because it was measured to have slightly higher beam current densities, and so higher erosion rates (Ref. 8). The photomicrographs of the screen webbing show that the ridge is centered with the webbing near the optics center, but the ridge shifts towards the grid center at larger radii. At even larger radii, the ridge is barely discernable. The photomicrographs also show deposition on the aperture walls and downstream surfaces, which will be discussed in the next section. Finally, Figure 7 shows cusps along the aperture walls that are artifacts of the manufacturing process. The NSTAR ELT thruster also exhibited a ridge that was centered with the webbing near the grid center, but shifted at larger grid radii (Ref. 21). However, it was unclear if the shifting was in a particular direction for the NSTAR thruster.

Screen grid thicknesses were measured from the webbing photomicrographs. Figure 8 shows the thicknesses as a function of radial location at the three locations indicated on the webbing image on the plot. Results are shown as a percentage of the estimated pretest thickness, which includes grid thinning as a result of the grid forming process. The smallest screen ridge thickness was 92 percent of the estimated pretest thickness. The smallest overall thickness was 86 percent of the estimated pretest thickness. Figure 8 further shows that the worst case erosion was off-center by about 6 cm. The off-center, worst case erosion may be an artifact of the annular-shaped, doubly-charged ion current density radial profile from the NEXT discharge chamber (Ref. 22). At 25 V, which is an approximate LDT discharge voltage, doubly-charged ions eroded the screen grid with a sputter yield that is 350 times that of singly charged ions (Ref. 23). As a result, doubly-charged ions can dominate screen grid erosion near the grid center where plasma densities are large. Regardless, because so little of the screen grid thickness was ultimately eroded during the 51.2 kh LDT, test results show that the NEXT screen grid has substantial service life remaining.

The NSTAR ELT screen grid webbing exhibited more erosion than that of the NEXT LDT grid (Ref. 21). However, the NSTAR peak beam current density at full power was significantly larger than that of the NEXT thruster at full power and screen grid webbing erosion tracked the beam current density profile. Peak beam current densities at full power were 5.9 mA/cm^2 for the NSTAR ELT thruster and 4.2 mA/cm^2 for the NEXT LDT thruster (Refs. 8 and 20). In addition, the double-to-single beam ion
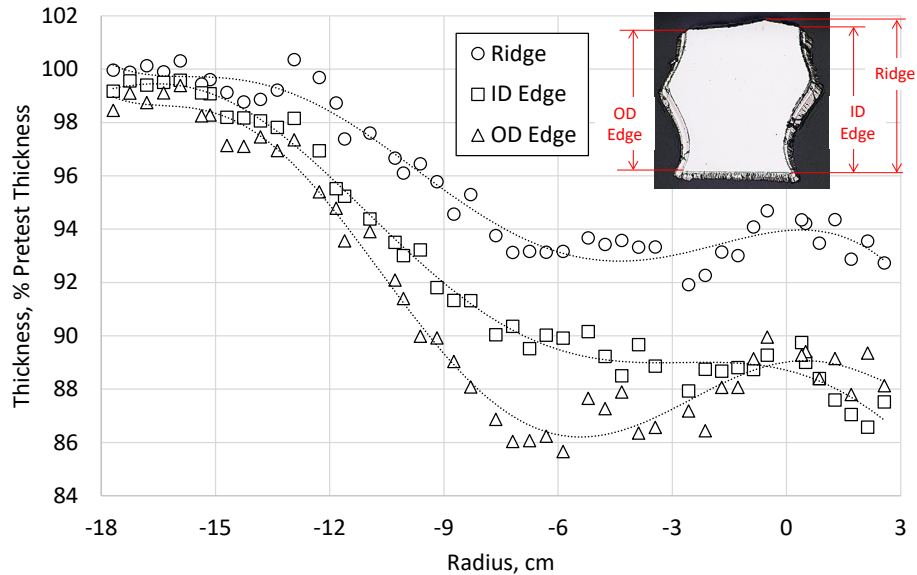
Figure 8.—Screen grid webbing thicknesses at three webbing locations as a function of radial location along radius B (see Figure 2). Thicknesses are shown as a percentage of the estimated pretest thickness. Thicknesses > 100 percent are due to measurement and pretest thickness estimate uncertainties.

current ratios for the NSTAR thruster at full power are about three times that of the NEXT LDT thruster at full power (Refs. 20 and 24). As a result, a higher degree of screen grid webbing erosion would have been expected for the NSTAR thruster.

4.2.2 Aperture Wall and Downstream Surface Deposition

As is evident in Figure 7, there was deposition on the screen grid aperture walls and downstream surfaces. The deposition was examined using a scanning electron microscope. A sample image of the aperture wall deposition that was created with backscattered electrons is shown in Figure 9. The constituents of the deposition were grid material and carbon with trace amounts of oxygen and trapped xenon propellant. The source of the grid material was likely dominated by accelerator aperture wall erosion products because of its proximity to the screen aperture walls and this is discussed below. The carbon was most likely back-sputtered carbon from the graphite panels lining the vacuum facility walls. The image shows both broad discolored bands and thinner whitish lines. The broad discolored bands are thought to have been formed during operation at the different throttle levels during LDT, where aperture wall erosion and back-sputtering rates were different. The darker bands furthest to the right and left of Figure 9 were likely formed during operation at full power, where back-sputtering was highest. The middle, lighter bands were likely formed during throttled operation between 13.0 and 29.2 kh. The thinner, whitish lines are grid material-rich layers that were likely formed during perveance measurements, where beam ions directly impinge the accelerator aperture walls and upstream surface and sputter-erode grid material at a higher rate.

The downstream surface deposition had very similar features as that of the aperture walls. The deposition was composed of the same constituents and exhibited similar discoloration bands indicative of extended operation at different throttle levels, as well as the whitish lines indicative of grid material-rich layers, likely due to perveance measurements. The only differences were that the discolored bands of full power operation had a higher grid material content and that the structure of the deposition was less continuous, exhibiting a unique growth pattern.
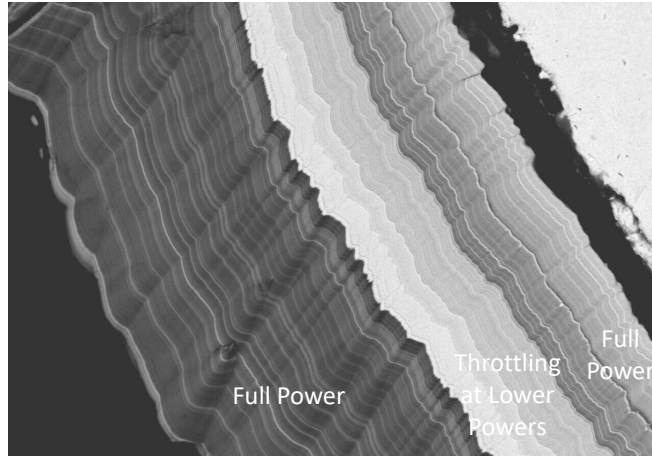
Figure 9.—Scanning electron microscope image of aperture wall deposition using backscattered electrons. The aperture was located at r = 0.4 cm along radius B. The darker regions are dominated by carbon while the lighter regions are dominated by grid material. The deposition separated from the grid substrate, likely during preparation of the cross section.

Aperture wall deposition thicknesses are shown in Figure 10 as a function of radial location. Deposition thicknesses on the ID and OD surfaces (i.e., the surfaces closest to and furthest from the ion optics center, respectively, as shown in Figure 10) are plotted separately. The figure shows that deposition thicknesses were ultimately a small percentage of the aperture diameter. In addition, deposition thicknesses were similar between ID and OD locations near the optics center. However, deposition thicknesses were larger on the ID surface at larger radii. This uneven deposition is most likely the result of non-uniform accelerator aperture wall erosion, which is discussed in the accelerator grid section. Accelerator aperture walls eroded unevenly due to a slight misalignment between the screen and accelerator apertures in the grid radial direction. As a result, the screen webbing ID surface collected more deposition because of its proximity to the erosion site of the accelerator aperture.

An interesting feature of the aperture wall deposition was the appearance of a slightly larger, partial ring at the upstream surface at the larger radii, which is shown in Figure 11. This partial ring-shaped deposition, which was a part of the aperture wall deposition, was non-uniformly distributed azimuthally about the aperture and was apparent for the mid- to outer-radius apertures. The center of the azimuthally non-uniform deposition pattern was aligned with the optics outer radius and the azimuthal extent of coverage increased with increasing grid radius from about 90° at mid-radius to 240° at 18 cm. The maximum protrusion of the deposition into the aperture was only about 4 percent of the nominal screen aperture diameter. An image of this deposition that was created with backscattered electrons is shown in Figure 12. The image shows that the partial ring deposition was predominantly formed during the second full power segment, following throttled operation (i.e., after 29.2 kh). Although the cause of this ring is presently unknown, the dominant carbon content of this deposition suggests that this was predominantly a facility effect. The impact of this deposition was a slightly reduced screen grid ion transparency during the second full power test segment, which is discussed later.
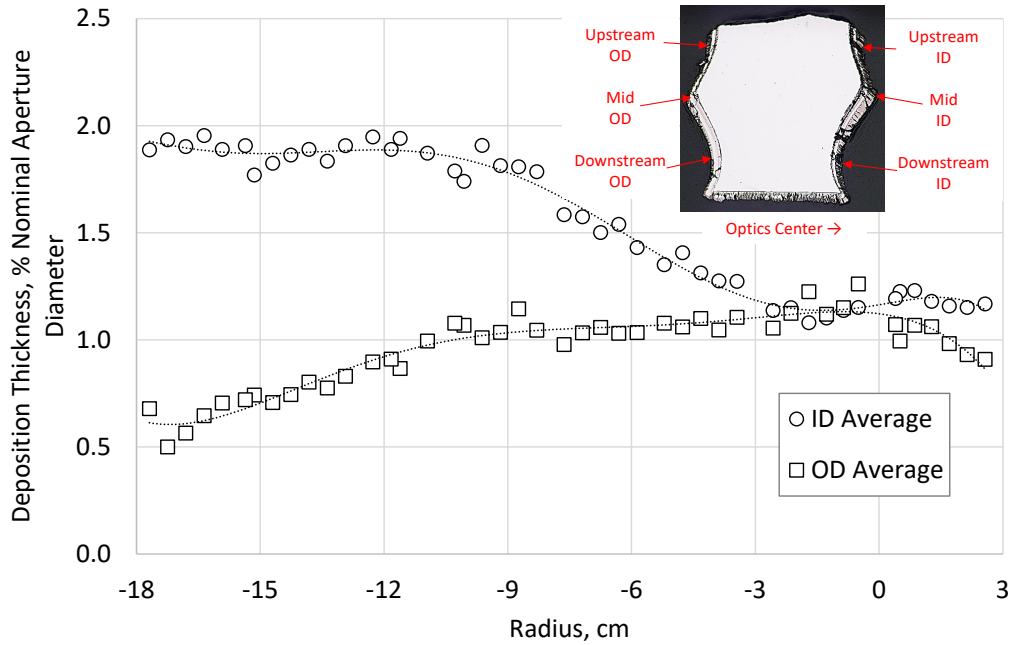
Figure 10.—Aperture wall deposition thicknesses as a function of radial locations along radius B (see Figure 2). Thicknesses are shown as a percentage of the screen grid aperture diameter. The image shows the three inner and outer diameter locations that were averaged and plotted in the graph.

Upstream, r = 10.8 cm (Radius A)   Upstream, r = 18 cm (Radius A)
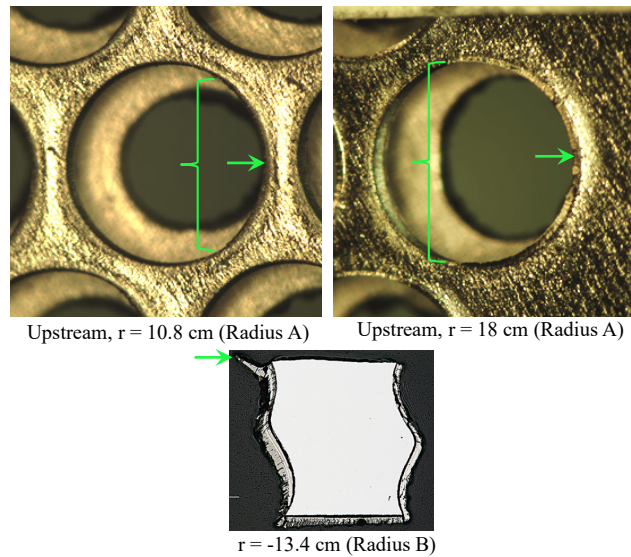
r = -13.4 cm (Radius B)

Figure 11.—Upstream screen aperture wall partial ring deposition. The green arrows indicate the deposition and the braces indicate the azimuthal extent of the deposition around the aperture. All images are oriented with the grid center to the left and the outer perimeter to the right.
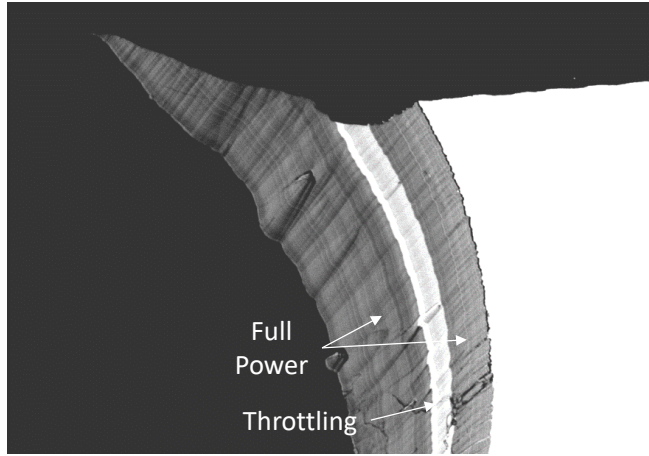
Figure 12.—Scanning electron microscope image of aperture
wall partial ring deposition using backscattered electrons.
The aperture was located at r = –16.4 cm along radius B.
The darker regions are dominated by carbon while the
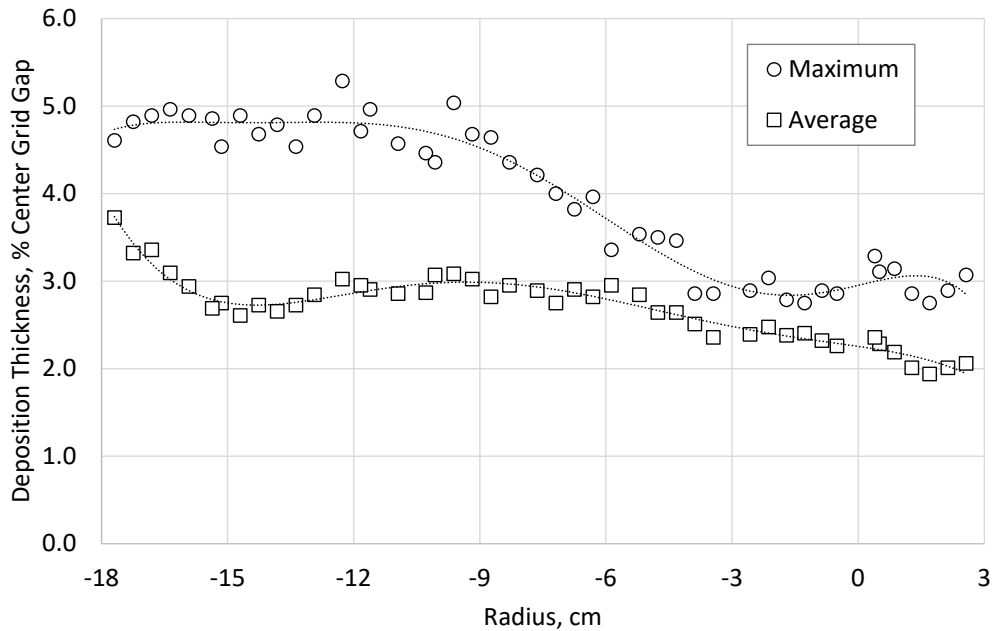lighter regions are dominated by grid material.

Figure 13.—Downstream webbing deposition thicknesses as a function of radial locations
along radius B (see Figure 2). Thicknesses are shown as a percentage of the cold grid
gap at the ion optics center. Three measurements at OD, middle, and ID locations were
averaged and plotted in the graph.

Downstream surface deposition thicknesses are shown in Figure 13 as a function of radial location.
The figure shows that deposition thicknesses were ultimately a small percentage of the cold grid gap.
Deposition thicknesses generally increased with increasing radius and the maximum thickness was on the
ID side at larger radii. As with aperture wall deposition, this uneven deposition is most likely the result of
the non-uniform accelerator aperture wall erosion discussed earlier. As a result, the downstream webbing
ID surface collected more deposition because of its proximity to the erosion site of the accelerator grid.
The maximum deposition thicknesses of Figure 13 were used to correct the measured cold grid gap data
to create Figure 4.

Throughout the post-test inspection of the screen grid, there was little evidence of the aforementioned screen grid deposition spalling off. The only deposition that was removed was at apertures where grid gap gages were used (which scraped off some of the deposition) and at rogue holes, where the partial ring deposition thickness became large. Regarding the latter, the spalled deposition at those sites was small and could have spalled during exposure to atmosphere. In addition, the partial ring was largely a facility effect. As a result, there was no evidence that the screen wall and upstream deposition created an electrical short.

4.2.3 Aperture Diameter Changes

The change in screen grid aperture diameters from pre- to post-test as a function of radius is shown in Figure 14. As the figure shows, aperture diameters decreased by 1.3 to 2.6 percent of the pretest values, with a 2.2 percent average decrease. Also shown in the figure is the total deposition on both cusps of an aperture measured along radius B. As the figure shows, the deposition on the cusps was responsible for the decrease in screen grid aperture diameters.
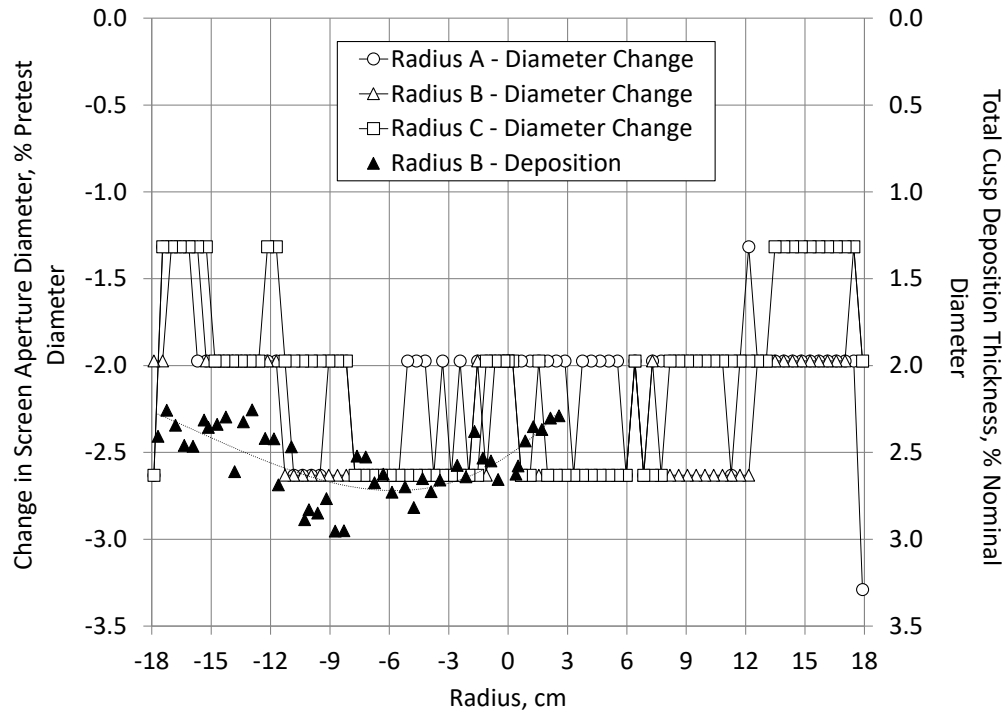

Figure 14.—Change in screen grid aperture diameter from pre- to post-test as a function of radial location along three optics radii. Also included is the screen aperture wall deposition measured along radius B (see Figure 2) at both cusps of an aperture. Aperture diameters were measured with pin gages in increments of 0.67 percent of the nominal screen aperture diameter. Changes in aperture diameter are expressed as a percentage of the pretest measurement and deposition thickness as a percentage of the nominal screen aperture diameter.

The reduced screen grid aperture diameters due to the deposition on the aperture walls and the partial ring deposition near the upstream surface would have been expected to reduce the measured screen grid ion transparencies during the NEXT LDT (Ref. 8). The reduction in aperture diameters was calculated to have decreased the screen grid open area fraction by 4.4 percent. The partial ring deposition for the outer apertures was calculated to have decreased the screen grid open area fraction by 2.5 percent. So, the total post-test screen grid open area fraction decreased by 6.8 percent. Screen grid ion transparency test data do indeed show a decrease over the duration of the LDT of 2 to 4 percent due to this decrease in the physical open area fraction of the screen grid, so the test data and post-test inspection measurements are consistent (Ref. 8). This was in contrast to the NSTAR ELT findings, where post-test screen aperture diameters had decreased as a result of similar deposition on the aperture walls, yet the screen grid ion transparency increased (Ref. 21).

4.2.4   Grid Mass Changes

The screen grid net mass loss was only 0.8 gm. However, part of the eroded mass was masked by the deposition mass. Based on the aforementioned erosion measurements, a preliminary estimate of mass loss due to erosion was about 5.2 gm. The mass of the deposition, however, was difficult to accurately estimate because the composition was a combination of grid material and carbon, and because the deposition density was unknown.

This estimated screen grid mass loss due to erosion was more than the 3.2 gm lost by the NSTAR ELT thruster. This was due in part to the larger beam extraction area and the longer duration of the test. Note, however, that the NEXT thruster operates at a lower doubly-to-singly-charged beam current ratio than the NSTAR thruster, which would have reduced its wear rates.

4.3   Accelerator Grid

Post-test inspections of the accelerator grid included both nondestructive and destructive inspection methods. Nondestructive inspection methods included photomicrographs of upstream and downstream surfaces and noncontact aperture diameter measurements. Destructive inspection included laser cutting the grid into smaller sections so that aperture webbing cross sections could be inspected with optical and scanning electron microscopes. Compositions were determined with energy dispersive x-ray spectroscopy. The following sections will present the results of those inspections. The first section will discuss downstream surface pit and groove erosion and its impact on service life. The second section will present the upstream surface erosion and aperture wall deposition. The third section will present aperture wall erosion results and its impact on performance. The section thereafter will discuss rogue holes. Finally, the change in accelerator grid mass will be evaluated.

4.3.1   Downstream Surface Erosion and Pits and Grooves

As discussed previously, the downstream accelerator grid surface exhibited net carbon deposition throughout most of the perforated diameter. Although there were some pit and groove erosion sites where the underlying grid material was exposed within the mid-radius area, very few of these net erosion sites were found. Most of these sites showed evidence of at least some net carbon deposition. In addition, all inspected accelerator grid aperture walls exhibited net carbon deposition.

The appearance of net carbon deposition on the accelerator aperture walls was expected because aperture wall wear rates decrease as the aperture enlarges (see, for example, Figure 5.3-2 of Ref. 21). The aperture would enlarge to the point where the decreasing ion flux eroding the walls is overcome by the back-sputtered carbon flux, leading to net carbon deposition. This temporal transition from net erosion to net deposition was confirmed with in situ images of the center aperture taken during the NEXT LDT. The

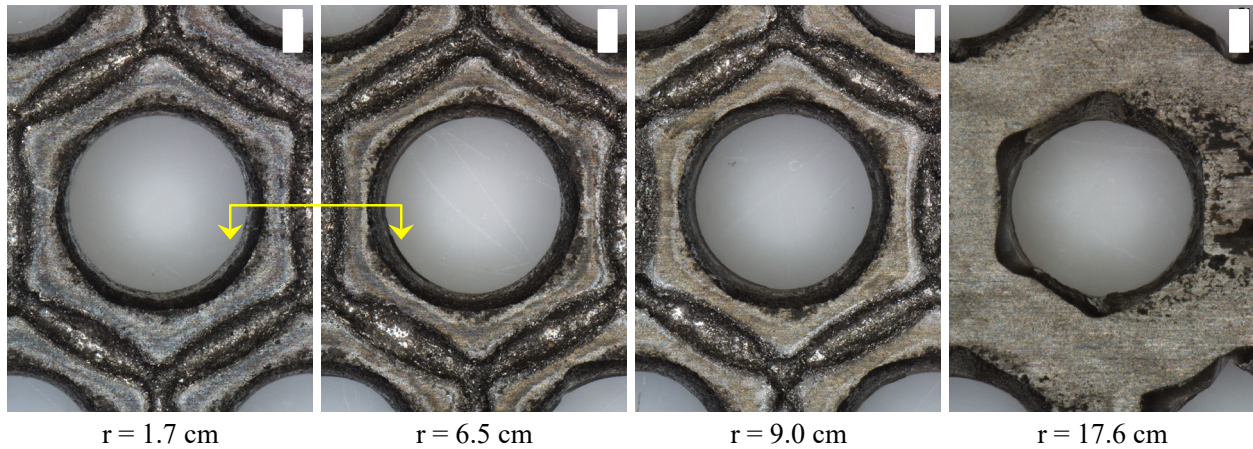| r = 1.7 cm | r = 6.5 cm | r = 9.0 cm | r = 17.6 cm |

Figure 15.—Post-test images of downstream accelerator grid apertures at various radial locations along radius A (see Figure 2) following soda blasting. All images are oriented with the optics center to the left and the outer perimeter to the right. The yellow arrows indicate the orientation of the webbing sections of Figure 17 relative to the ion optics center.

appearance of net carbon deposition in the pit and groove erosion pattern on the downstream surface was, however, unanticipated. An investigation of this finding, which is described in the Appendix, revealed that net erosion of the pit and groove erosion at locations within about mid-radius persisted through 36.5 kh.

Because the carbon deposits obscured measurements of post-test erosion, the deposition on the accelerator grid was removed from several grid sections using a soda blasting process. Images of the resulting accelerator grid downstream surfaces are shown in Figure 15 at various radial locations. Evident in the images is the pit and groove erosion sites on the downstream surfaces except for the outer most apertures, where the erosion fades away at larger radii due to masking by back-sputtered carbon (Ref. 25). Also evident in the figure is the chamfering of the downstream aperture walls that was measured as a function of time for several apertures. This circular chamfering transitions to a hexagonally star-shaped erosion pattern for the outer radius apertures, which will be quantified in a later section.

A cross section of a pit and groove erosion pattern is show in Figure 16 for a grid section whose deposition was also removed. An interesting feature of the pit and groove erosion pattern is that although the depths of the pits and groove appear similar, a careful inspection shows that the grooves are actually deeper than the pits. This was unlike the NSTAR ELT thruster operating conditions, which produced pit depths that were far greater than groove depths (Refs. 19 and 21). To quantify the depth of the grooves, the accelerator grid webbing was sectioned at the middle of a web for inspection as shown in Figure 15. The grid sections were mounted in epoxy prior to polishing to reduce the amount of grid deposition removed during the preparation process. Sample accelerator grid webbing cross sections are shown in Figure 17 at various radial locations. The grid was sectioned along radius B of Figure 2 because this radius most closely tracked the beam current density measurements. In addition, most measurements were made along the negative radius side because it was measured to have slightly higher beam current densities, and so it was anticipated to have higher erosion rates (Refs. 8). Although the deposition was not purposely removed for these sections, spalling had occurred prior to and during the preparation process, so some downstream sites exhibited deposition while others did not.
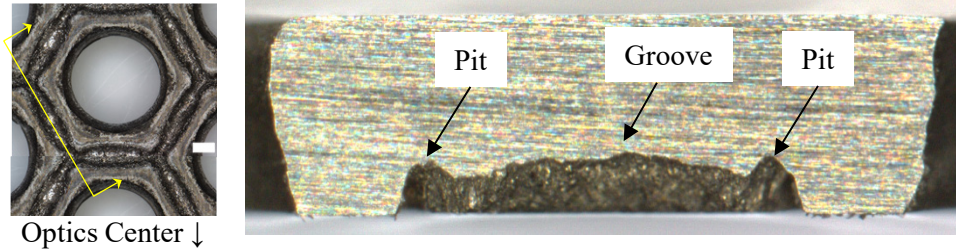
Figure 16.—Post-test photomicrograph of a sectioned and polished accelerator grid webbing at a radius of about 6.3 cm near radius B (see Figure 2). The yellow lines and arrows on the image to the left indicate the orientation of the sectioning.

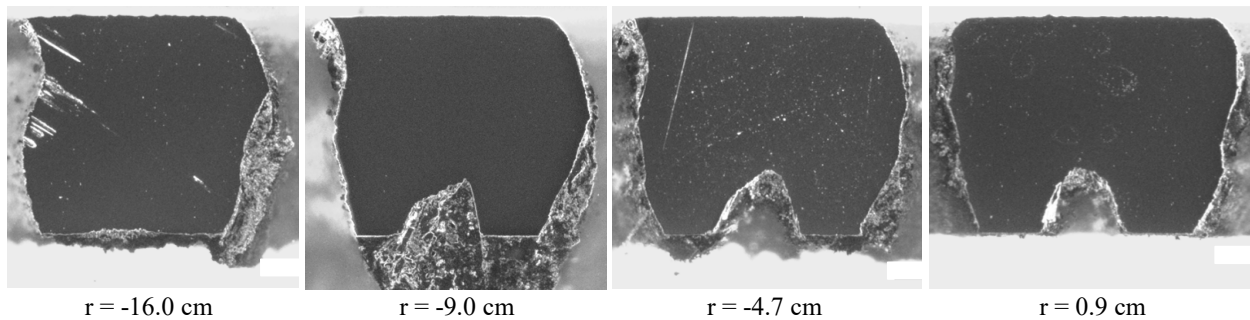| r = -16.0 cm | r = -9.0 cm | r = -4.7 cm | r = 0.9 cm |

Figure 17.—Photomicrographs of accelerator grid webbing cross sections at various radial locations along radius B (see Figure 2). Figure 15 shows the orientation of the grid sectioning. All images are oriented with the optics center to the right and the outer perimeter to the left; the bottom surfaces are the downstream surfaces. The solid, dark central regions are the grid webbing substrate and the grayish material surrounding the webbing is deposition.

Figure 17 shows many important features of erosion and deposition. The upstream surfaces showed little erosion. Erosion of the aperture walls was asymmetric away from the optics center such that there was net deposition evident on the outer diameter side of the webbing while there was net erosion of the inner diameter side. The downstream surfaces next to the grooves were uneroded, likely due to net carbon deposition on those surfaces early in testing. Lastly, net carbon deposition was porous, resulting in ridges surrounding the pit and groove erosion pattern that were measured to be as large as about 70 percent of the grid thickness by the end of the test.

Accelerator groove dimensions were measured using the webbing photomicrographs of Figure 17. Groove widths were measured to be 27 to 43 percent of the nominal grid thickness, and the widths were independent of radius. Figure 18 shows groove depths as a function of radius. Results are shown as a percentage of the estimated pretest thickness, which included the grid thinning as a result of the grid forming process. The graph shows that groove depths were 27 to 35 percent of the grid thickness out to a radius of about 6 cm and decreased substantially at the measured locations of transition from net erosion to net carbon deposition at full power (Ref. 25).

The maximum measured groove depth of 35 percent of the grid thickness was about half that estimated with in situ diagnostics, so this discrepancy was investigated. Although the in situ measurement technique suffered from a number of inaccuracies, the most significant appeared to be the lack of an adequate reference plane (Ref. 24). Most measurements were averages of distances from the groove to the downstream and upstream grid surfaces. Unfortunately, the downstream grid surface was masked by porous carbon deposition that grew to a substantial thickness relative to the grid thickness. And the upstream accelerator aperture edge had eroded (see the inner diameter edges of Figure 17). Therefore during the LDT, both reference planes shifted in a manner that exaggerated the true depth of the eroded grooves.
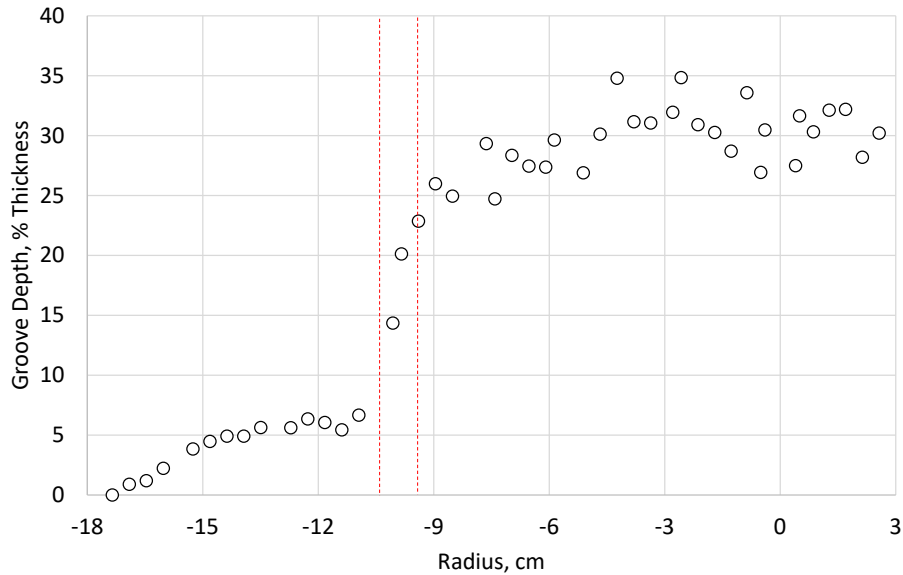
Figure 18.—Accelerator grid groove depths as a function of radial location along radius B (see Figure 2). Depths are shown as a percentage of the estimated pretest thickness. The red dotted lines indicate the measured transitions from net erosion to net deposition at 10.7 cm at the end of the first full power test segment (i.e., 13.0 kh) and 9.4 cm during the second full power test segment (i.e., 36.5 kh) (Ref. 25).

The maximum measured groove depth was also about half that estimated by a semi-empirical model (Refs. 4 and 5). This model predicted erosion through about 75 percent of the grid thickness by 36 kh, after which net carbon deposition had occurred, masking this erosion site (Ref. 24). This discrepancy is still under investigation, but preliminary findings include model oversimplifications, such as ignoring the redistribution of erosion within the pit and groove pattern at throttled conditions during the LDT.

More pit and groove erosion measurements are presently being made at different locations on the grid. This will help to verify the true deepest groove erosion sites and to establish the service life of the thruster based on this failure mode.

4.3.2 Upstream Surface Erosion and Aperture Wall Deposition

Post-test images of the upstream accelerator apertures following soda blasting are shown in Figure 19 at various radial locations. The images show a slight chamfering of the upstream aperture walls near the center of the grid. But at larger radii, the images also show preferential erosion towards the outer radius of the ion optics. This same erosion pattern was confirmed by inspecting accelerator apertures along other optics radii and by comparing pre- and post-test aperture alignment images. This preferential erosion of an accelerator aperture wall towards the outer radius, referred to as "notching" herein, is the result of a minor systemic misalignment between screen and accelerator aperture pairs in the radial direction of the ion optics. The notched erosion pattern forms as beam and charge exchange ions are preferentially accelerated into those accelerator aperture surfaces closest to the centerline of the screen aperture.

The result of this misalignment is non-axisymmetric accelerator aperture wall erosion, which is evident in webbing images of Figure 17 for apertures away from the ion optics center. The webbing surfaces closest to the optics outer perimeter of a given aperture show a chamfered erosion pattern while the opposite surface shows little or no erosion. In addition, the latter surface exhibits net deposition, which is evident in Figure 17. The deposition at these locations was examined using a scanning electron microscope. The constituents of the deposition were grid material and carbon. Also evident in the images produced with backscattered electrons were broad discolored bands indicative of throttling during the

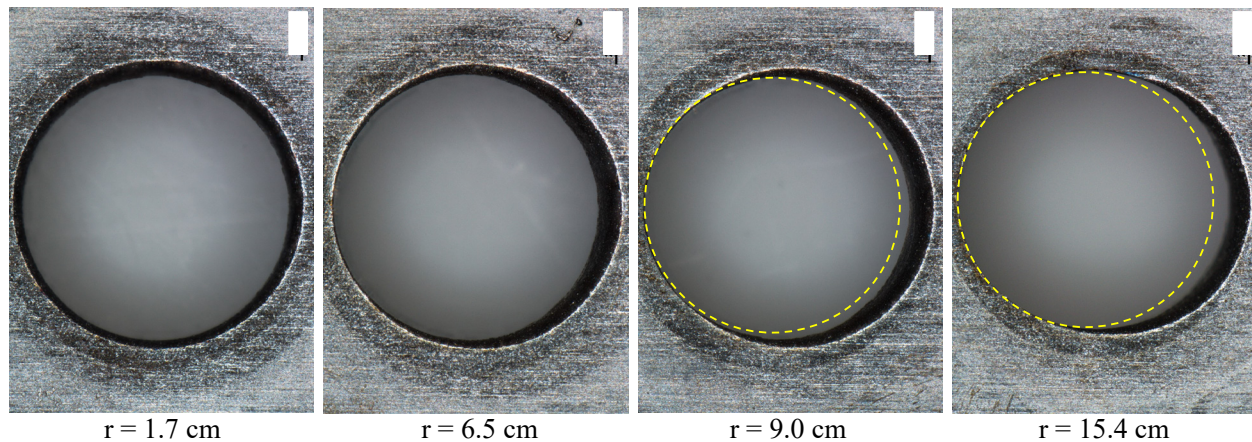| r = 1.7 cm | r = 6.5 cm | r = 9.0 cm | r = 15.4 cm |

Figure 19.—Post-test images of upstream accelerator grid apertures following soda blasting at various radial locations along radius A (see Figure 2). All images are oriented with the grid center to the left and the outer perimeter to the right. The dashed yellow circles indicate the approximate pretest aperture.

LDT and thinner whitish lines, similar to that of the screen grid deposition (see Figure 9). The thickness of the deposition was also measured at various radial locations. It was found to vary, reaching peak values between the optics center and mid-radius apertures of 13 percent of the grid nominal thickness. Also, there were sites on the upstream accelerator grid where this deposition was found to have spalled, though it is unclear if this was the result of atmospheric exposure or post-test handling. Regardless, the majority of the deposited material's atomic composition was measured to be carbon, which is a facility effect that would not be present in a spaceflight application.

The asymmetric deposition thicknesses on the screen grid aperture walls and upstream surfaces were also the result of this accelerator aperture notching erosion. Screen grid surfaces closest to the notched erosion sites exhibited the thickest deposition layers, which is indicative of the depositing material's origin. That the deposition on the non-eroded accelerator aperture walls exhibits similar compositions is a further indication that the depositing material originated from the same source.

In addition to notching erosion, aperture misalignment also deflects the thrust-producing beam ions towards the accelerator surface closest to the screen aperture centerline (Ref. 26). As a result, beam ions are deflected towards the closer accelerator grid surface. For the NEXT LDT ion optics, Figure 19 indicates that beam ions would have been deflected radially outward at beginning of life. However, the accelerator aperture surfaces producing the deflections receded as they eroded, which would then produce less beam ion deflection as a function of time. This anticipated temporal behavior is the likely explanation for the change in beam current density profiles between the start and end of the test (Ref. 8). By the end of the LDT, beam current density profiles measured by the two furthest downstream planar probes were more peaked near the center and the profile "shoulders" were less pronounced, both of which were indicative of a more collimated beam. This likely occurred because beam ions experienced less deflection by the end of the test due to accelerator aperture notching erosion.

Because this misalignment would have deflected beam ions off axis, the thrust would have been expected to be lower at beginning of life. This effect was modeled by assuming that apertures were aligned at the end of the test and the eroded images of Figure 19 were used to determine beginning of life misalignment. The result was a thrust increase at the end of the LDT of 0.5 percent at full power. It is unlikely that a thrust measurement would have been able to discern such a small change throughout the LDT.

These results indicate that although changes in aperture alignment as a result of the earlier NEXT 2000 h wear test reduced notching erosion, they were still not enough (Ref. 6). The resolution to this minor misalignment is straightforward. Screen and accelerator aperture pairs are set during manufacture to yield a particular alignment. This can easily be adjusted to account for the misalignment noted in this section. Doing so can mitigate any potential concerns regarding deposition, spalling, and performance.

4.3.3   Aperture Enlargement

Post-test aperture diameters as a function of radial location are shown in Figure 20 for the minimum diameters and in Figure 21 for the downstream and upstream surface diameters. For both figures, non-contact methods were used to make these measurements. Also included in both figures are in situ measurements for the ion optics center aperture and an aperture at a radius of 16.3 cm. All results are shown as changes relative to the measured pretest diameters, which were within ± 2 percent of the average diameter. The tighter manufactured tolerances of the pretest PM accelerator aperture diameters represented a significant improvement over prior NEXT accelerator grids (Ref. 6).

Figure 20 shows that post-test aperture minimum diameters with deposition removed with soda blasting grew by about 5 percent of the pretest value at the outer radius to about 7 percent of the pretest value near the center. According to in situ measurements, these diameter increases occurred during operation at throttled power levels between 13.0 and 29.2 kh. This is an indication that operation at full power for the NEXT thruster did not significantly increase the minimum diameter, although this is not the case for the upstream and downstream surfaces, which is discussed later in this section. The increases in minimum diameters were smaller than those of the NSTAR ELT thruster. NSTAR ELT post-test accelerator apertures diameters increased by as much as 24 percent of the pretest measurements (Ref. 21).
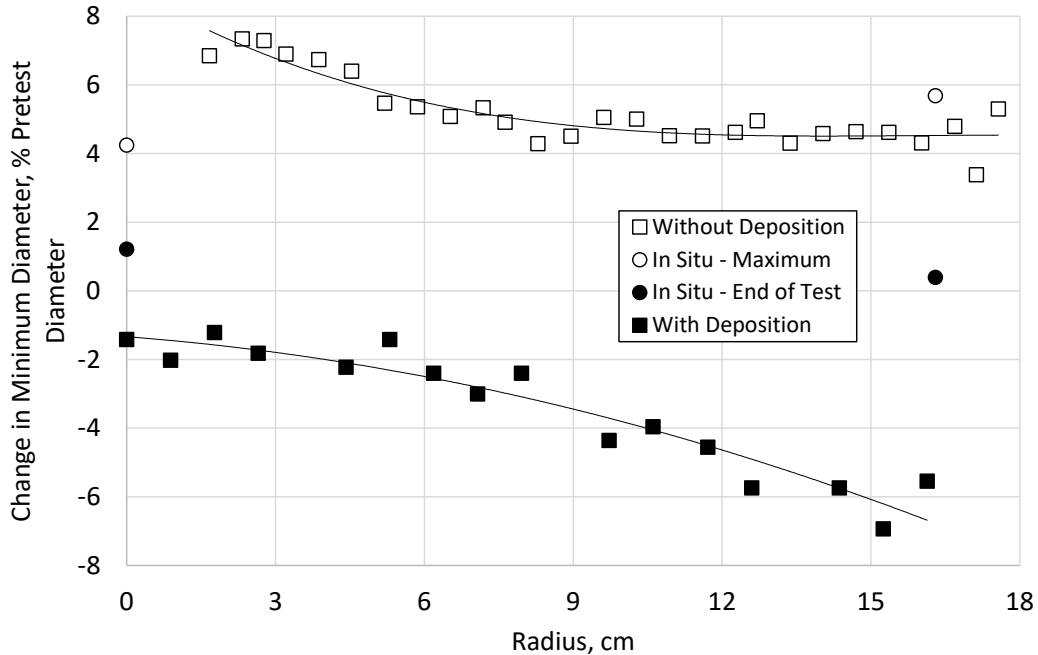

Figure 20.—Change in accelerator grid aperture minimum diameter from pre- to post-test as a function of radial location along radius A (see Figure 2). Also included are the maximum and end of test in situ measurements. Changes in aperture diameter are expressed as a percentage of pretest measurements.
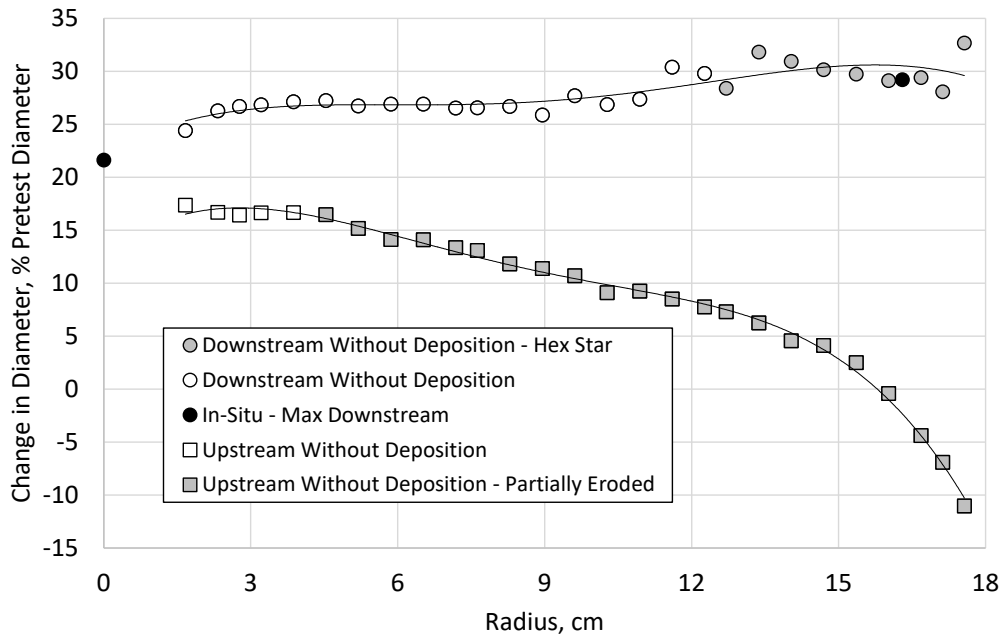
Figure 21.—Change in accelerator grid aperture downstream and upstream surface diameter from pre- to post-test as a function of radial location along radius A (see Figure 2). Also included are the maximum and end of test in situ measurements. Changes in aperture diameter are expressed as a percentage of pretest measurements.

This was likely due to the larger beam current densities of the NSTAR ion thruster and smaller pretest diameters compared to NEXT. Peak beam current densities at full power were 5.9 mA/cm^2 for the NSTAR ELT thruster and 4.2 mA/cm^2 for the NEXT LDT thruster (Refs. 8 and 20). This and the 11 percent larger beginning of life NEXT accelerator aperture diameters led to modest minimum diameter enlargement of the NEXT LDT ion optics (Ref. 5).

Figure 20 also shows the post-test change in minimum diameter with deposition as a function of radius. The diameter decrease was the result of net carbon deposition within the apertures. This was also evident with in situ measurements, which indicated that net carbon deposition impacted the minimum diameter between 38 and 42 kh. Figure 20 also includes comparisons with in situ measurements. The differences between in situ end of test measurements and the post-test results with deposition were due to the method of determining the diameter. In situ diameters were determined by averaging numerous diameter measurements while post-test diameters were the largest circle that would fit within the aperture. The latter would produce a conservative result due to the uneven deposition of material within the aperture walls.

Figure 21 shows that post-test aperture downstream surface diameters with deposition removed by soda blasting grew by about 24 to 33 percent of the pretest values. According to in situ measurements for the center aperture, the increase in downstream surface diameter occurred predominantly during the first full power test segment (i.e., to 13.0 kh). For the in situ measurement of the aperture at 16.3 cm, the increase in downstream surface diameter occurred during the first full power segment and most of the throttling segments (i.e., from 13.0 to 29.2 kh). For radial locations ≥ 12.7 cm, the downstream surface further exhibited a hexagonal star-shaped erosion pattern (e.g., see Figure 15, r = 17.6 cm) similar to that found in Reference 6, though not as severe. These results suggest that increasing the accelerator aperture diameters, improving manufacturing tolerances, and masking down the perforated diameter from 40 to 36 cm were successful in reducing the degree of accelerator aperture erosion at the lower beamlet currents at larger radii (Ref. 6).

Figure 21 also shows upstream surface erosion at various radial locations. These diameters also increased by about 17 percent of the pretest minimum diameters near the optics center. However at radii ≥ 4.5 cm, only part of the upstream surface was eroded due to aperture misalignment (e.g., see Figure 19, r = 15.4 cm), and the diameter of this eroded surface decreased with radius to values less than the pretest minimum aperture diameters. Figure 21 also shows that in situ measurements matched those measured post-test.

Aperture diameter changes largely impacted ion optics performance parameters that included screen grid ion transparency, perveance limit, electron backstreaming limit, and accelerator current (Ref. 8). Screen grid ion transparencies were thought to have been strongly influenced by deposition on the screen grid aperture walls as discussed earlier. The perveance limit was likely influenced by the minimum aperture diameter. As the minimum aperture diameter increased due to erosion, the perveance limit decreased (i.e., improved) until about 29 to 36 kh (Ref. 8). Thereafter, the perveance limit increased, likely due to net carbon deposition within the aperture walls. This is similar to in situ measurements, but they showed diameter decreases after 38 to 42 kh, so there is a temporal discrepancy. Electron backstreaming limit trends did not track the minimum aperture diameter trends as would have been expected (Ref. 8). Although further modeling is required, electron backstreaming may also have been influenced by neutralizer performance and net carbon deposition on the downstream surfaces, both of which can improve the limits, especially during the first 30 kh of the LDT (Ref. 8).

4.3.4 Rogue Holes

During the NEXT LDT, a careful inspection of ion optics long range images showed four accelerator apertures whose shape was deformed by erosion. Their approximate locations are shown in Figure 2 and are labeled (a) to (d). The erosion of these apertures, referred to as "rogue holes," was likely caused by debris on the corresponding screen aperture. The debris deformed the upstream sheath and deflected beam ions into the walls of the accelerator aperture. Following the test, the rogue apertures were located and carefully inspected, especially aperture (a) whose diameter approached that of the screen aperture diameter. Interestingly, the corresponding screen apertures exhibited excessive deposition on the aperture walls that is non-uniform azimuthally (i.e., partial ring deposition) and showed some signs of spalling. However, this was not the cause of the rogue hole but likely a result of the erosion. In addition, the rogue holes were identified at 29.4 kh, which was prior to the formation of the partial ring deposition. The debris that likely caused the rogue holes are believed to have been removed some time during the LDT. The rogue holes had no noticeable impact on ion optics performance.

4.3.5 Grid Mass Changes

The accelerator grid net mass loss was 29.5 gm. However, part of the eroded mass was masked by the deposition mass, and scanning electron microscopy of the deposition showed that it was composed of porous carbon and grid material. The mass of the grid deposition was estimated by measuring the change in mass of the Figure 17 grid segments before and after deposition removal. The resulting mass removal as a function of radius was integrated over the area of the grid assuming axisymmetric deposition. The estimated deposition mass for the accelerator grid was 12.4 gm. This result does not include the deposition on the unperforated region of the grid, and the soda blasting did not remove all material from the pit and groove erosion pattern. So, the deposition mass was likely even larger. A preliminary estimate of accelerator grid mass loss due to erosion is about 41.9 gm.

This estimated accelerator grid mass loss due to erosion was more than the 33.7 gm lost by the NSTAR ELT thruster. This is not surprising given the longer test duration and higher beam currents for the NEXT LDT. Future NEXT LDT net accelerator grid erosion estimates should include the deposition on the unperforated region of the grid.

5.0   Summary

A Long Duration Test was initiated in June 2005 as a part of the NASA's Evolutionary Xenon Thruster (i.e., NEXT thruster) service life validation approach. Testing was voluntarily terminated in February 2014, with the thruster accumulating 51,184 hours of operation, processing 918 kg of xenon propellant, and delivering 35.5 MN-s of total impulse. The post-test inspection objectives were derived from the original NEXT LDT test objectives and expanded to encompass other goals. A primary objective of the post-test inspection of the ion optics is to measure the wear rates of critical surfaces and potential spalling sources and use these results to verify and update service life models. Expanded objectives included verification of in situ measurements, verification and resolution of issues and concerns during the nine year test, verification of part design improvements, and the identification of any unanticipated thruster life-limiting phenomena.

Regarding the ion optics assembly, post-test impedances of the individual insulators indicated no degradation with operation. All ion optics assembly threaded fastener breakaway torques were still preloaded. The cold grid gap had decreased by 2 to 13 percent of pretest center grid gap, with an average of all measurements of 7 percent of pretest center grid gap. This is substantially less than the 30 percent decrease measured for the NSTAR thruster following the ELT (Ref. 19), so efforts to stabilize NEXT ion optics grid gap changes were largely successful.

The upstream screen grid surface exhibited a chamfered erosion pattern that is very similar to that of the NSTAR thruster that was measured following the ELT (Ref. 19). The smallest screen ridge thickness was 92 percent of the estimated pretest thickness and the smallest screen grid thickness near an aperture wall was 86 percent. Because so little of the screen grid thickness was ultimately eroded during the 51.2 kh LDT, test results show that the NEXT screen grid has substantial service life remaining.

Deposition was found on the screen aperture walls and downstream surfaces that was primarily composed of grid material and carbon. The source of the grid material was likely accelerator aperture wall erosion because of its proximity to the screen aperture walls and the carbon was most likely back-sputtered facility material. Scanning electron microscopy showed broad discolored bands that could be traced to operation at the different throttle levels during LDT. Deposition thicknesses were ultimately a small percentage of the aperture diameter and grid gap. There was little evidence of this deposition spalling off, so it is unlikely that the screen wall and upstream deposition created an electrical short. The aperture wall deposition decreased screen grid aperture diameters by 1.3 to 2.6 percent of pretest values and was calculated to have decreased the screen grid open area fraction by 6.8 percent. This likely caused the 2 to 4 percent screen grid ion transparency decrease during the NEXT LDT.

The screen grid net mass loss was only 0.8 gm. However, part of the eroded mass was masked by the deposition mass. A preliminary estimate of mass loss due to erosion was about 5.2 gm. This estimated screen grid mass loss due to erosion was more than the 3.2 gm lost by the NSTAR ELT thruster due in part to the larger beam extraction area and the longer duration of the NEXT LDT.

The downstream accelerator grid surface and aperture walls exhibited net carbon deposition throughout most of the perforated diameter. The appearance of net carbon deposition on the accelerator aperture walls was expected because of decreasing aperture wall wear rates as the surface recedes. However, the appearance of net carbon deposition in the pit and groove erosion pattern on the

downstream surface was unanticipated. An investigation revealed that net erosion of the pit and groove erosion at locations within about mid-radius persisted through 36.5 kh.

An interesting feature of the pit and groove erosion pattern was that the grooves are slightly deeper than the pits. Groove depths were 27 to 35 percent of the grid thickness out to a radius of about 6 cm and decreased at the measured locations of transition from net erosion to net carbon deposition at full power. The groove depth discrepancy with in situ measurements made during the LDT was likely due to the lack of an adequate reference plane that exaggerated the depths. The discrepancy with a semi-empirical model is under investigation. More pit and groove erosion measurements are presently being made at different locations on the grid.

Upstream accelerator grid erosion showed preferential erosion towards the outer radius of the ion optics at larger radii, referred to as notching, and was the result of a minor systemic misalignment of grid aperture pairs in the radial direction of the ion optics. Erosion images showed that beam ions would have been deflected radially outward at beginning of life, but this would have diminished as the aperture eroded. This temporal behavior is the likely explanation for the change in beam current density profiles between the start and end of the test. The resolution to this minor misalignment is a straightforward adjustment.

Post-test aperture minimum diameters increased only by about 5 to 7 percent of the pretest values and in situ measurements indicate that this change occurred during operation at throttle power conditions between 13.0 and 29.2 kh. The increases in minimum diameters were smaller than those of the NSTAR ELT thruster, likely due to the larger beam current densities and smaller aperture diameters of the NSTAR ion thruster. Post-test NEXT LDT aperture downstream surface diameters grew by about 24 to 33 percent of the pretest diameters and in situ measurements indicate that the increase occurred predominantly during the first full power test segment (i.e., to 13.0 kh). For radial locations ≥ 12.7 cm, the downstream surface further exhibited a hexagonal star-shaped erosion pattern similar to that found in the NEXT 2000 h wear test, though not as severe. These results suggest that increasing the accelerator aperture diameters, improving manufacturing tolerances, and masking down the perforated diameter from 40 to 36 cm were successful in reducing the degree of accelerator aperture erosion at larger radii.

The accelerator grid net mass loss was 29.5 gm. Accounting for the mass of the deposition, a preliminary estimate of accelerator grid mass loss due to erosion was about 41.9 gm. This was more than the 33.7 gm lost by the NSTAR ELT thruster. This is not surprising given the longer test duration and higher beam currents for the NEXT LDT.

Appendix

The appearance of net carbon deposition in the accelerator grid's pit and groove erosion pattern on the downstream surface was unanticipated. Unlike aperture wall erosion, downstream grid surface erosion rates were anticipated to be constant with time and the back-sputter carbon flux was measured to be unchanged by the end of testing (Refs. 8 and 25). Because net carbon was deposited within this erosion site, erosion of the underlying grid material was inhibited, masking the eventual failure mode caused by this wear mechanism. The masking of this failure mode at some point during the LDT does not impact the service life capability of the thruster, but only impacts the service life verified via test for this failure mode. Because of its significance to thruster service life verification, an investigation was undertaken to determine both when net carbon deposition occurred within this erosion site and why.

The NEXT LDT was equipped with in situ cameras that could image the accelerator grid apertures throughout the test. The cameras that image the aperture and cold grid gap at the ion optics center could potentially be used to evaluate when net carbon deposition had occurred within the pit and groove erosion pattern. Unfortunately, the lighting for the cameras was severely degraded at 30.8 kh and this severely limited the quality of the images thereafter. Figure 22 shows an image of the center aperture just prior to the failure of the imaging system's lighting. This image, and all images prior to this time, show net erosion within the pit and groove erosion pattern. The darker areas within the erosion pattern are due to shadowing from the surrounding walls and the granular texture of the eroded grid surface. Following the lighting system degradation, attempts were intermittently made to illuminate the erosion pattern using external lighting. Figure 22 also shows the latest images following the lighting system degradation when the external lighting was sufficient enough to illuminate the pits and grooves erosion pattern. The images taken at 34.1 and 35.6 kh only show some of the groove pattern, but the visible grooves show no net carbon deposition.

The thruster and accelerator grid were also imaged at long range through a vacuum facility view port located at the facility end opposite the thruster. These images, taken intermittently throughout the test, were reviewed to determine when net deposition had occurred. Figure 23 shows long-range accelerator grid images that bracket when net carbon deposition had occurred. The image taken at 36.5 kh shows net erosion within the grooves erosion pattern, while the image taken at 41.5 kh shows that net carbon deposition had occurred. And although the 36.5 kh image shows net erosion, the net erosion pattern is not uniform. Specifically, most of the pits and some grooves exhibited net carbon deposition. This may be indicative that the process that led to net carbon deposition had begun at or just prior to 36.5 kh.

To understand the root cause for the net deposition within the pit and groove erosion sites, long range images were further evaluated. These images of the accelerator grid show that during the second full power segment (i.e., after 29.2 kh), the transition radius from net erosion to net deposition increased. During full power operation at 41.6 kh, the net erosion area was an annulus, with the grid center exhibiting net deposition as shown in Figure 24. This is in contrast to the end of the first full power test segment at 13.0 kh, also shown in Figure 24. Because neither the back-sputter rate nor the accelerator current had changed (Ref. 8), the only known mechanism that could have caused this was a change in accelerator current density distribution across the downstream surface of the grid. Unfortunately, the cause for this change is presently unknown.

Regardless, in situ and long range images confirm that erosion of the pit and groove erosion site persisted until 36.5 kh, which corresponded to a propellant throughput of 621 kg.

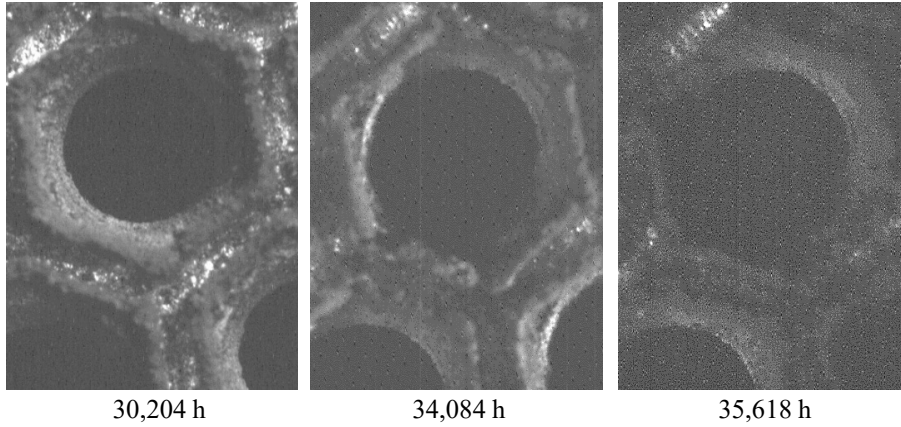30,204 h   34,084 h   35,618 h

Figure 22.—In situ center accelerator grid aperture images taken at 30,204, 34,084, and 35,618 h. The image at 30,204 h was taken just prior to degradation of the imaging system's lighting. The dark gray structures surrounding the pits and grooves and on the aperture walls are back-sputtered carbon. External lighting was used to obtain the two images to the right.
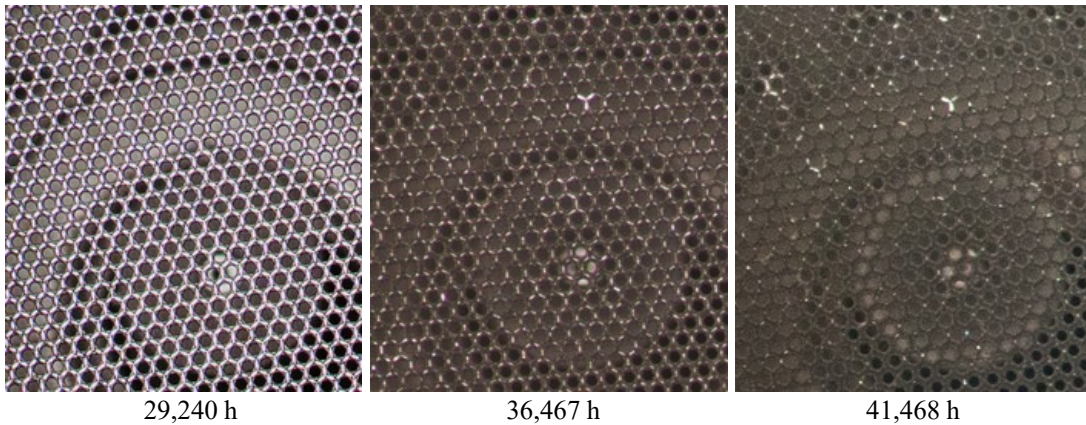

29,240 h   36,467 h   41,468 h

Figure 23.—Long-range images of the accelerator grid. The images were taken at 29,240, 36,467, and 41,468 h. The discharge cathode assembly is visible behind the grids.
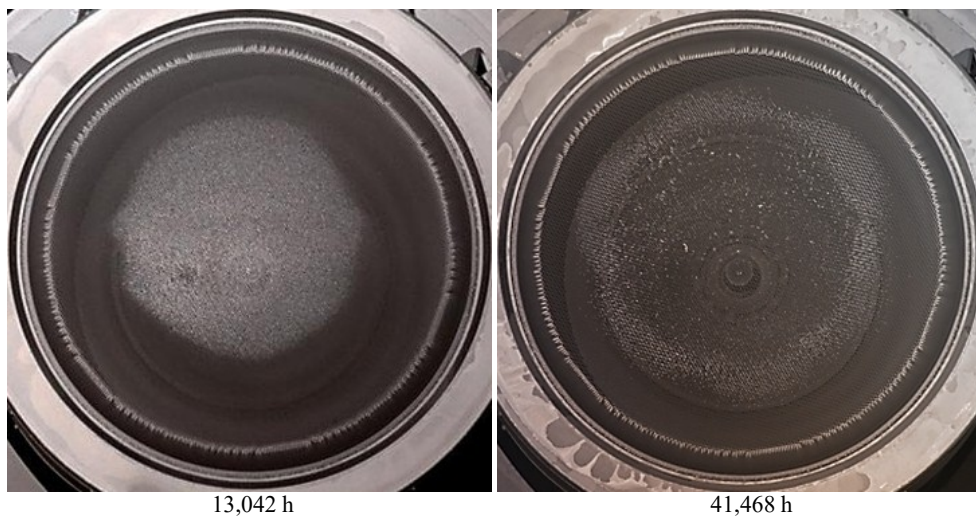

13,042 h   41,468 h

Figure 24.—Long-range images of the accelerator grid. The images were taken at 13,042 h at the end of the first full power segment and at 41,468 h during the second full power segment. The discharge cathode assembly is visible behind the grids. Note the larger diameter annulus of net erosion at 41,468 h.

References

1. Patterson, M.J. and Benson, S.W., "NEXT Ion Propulsion System Development Status and Performance," 43rd AIAA/ASME/SAE/ASEE Joint Propulsion Conference and Exhibit, AIAA-2007-5199, Cincinnati, OH, July 8–11, 2007.

2. Garner, C.E. and Rayman, M.D., "In-Flight Operation of the Dawn Ion Propulsion System Through Survey Science Orbit at Ceres," 51st AIAA/SAE/ASEE Joint Propulsion Conference, AIAA-2015-3717, Orlando, FL, July 27–29, 2015.

3. Polk, J.E., et al., "Demonstration of the NSTAR Ion Propulsion System on the Deep Space One Mission," 27th International Electric Propulsion Conference, IEPC-2001-075, Pasadena, CA, October 15–19, 2001.

4. Van Noord, J.L., "Lifetime Assessment of the NEXT Ion Thruster," 43rd AIAA/ASME/SAE/ASEE Joint Propulsion Conference and Exhibit, AIAA-2007-5274, Cincinnati, OH, July 8–11, 2007.

5. Van Noord, J.L. and Herman, D.A., "Application of the NEXT Ion Thruster Lifetime Assessment to Thruster Throttling," 44th AIAA/ASME/SAE/ASEE Joint Propulsion Conference and Exhibit, AIAA-2008-4526, Hartford, CT, July 21–23, 2008.

6. Soulas, G.C., Kamhawi, H., Patterson, M.J., Britton, M.A., and Frandina, M.M., "NEXT Ion Engine 2000 Hour Wear Test Results," 40th AIAA/ASME/SAE/ASEE Joint Propulsion Conference and Exhibit, AIAA-2004-3791, Fort Lauderdale, FL, July 11–14, 2004.

7. Van Noord, J.L., Soulas, G.C., and Sovey, J.S., "NEXT PM1R Ion Thruster and Propellant Management System Wear Test Results," 31st International Electric Propulsion Conference, IEPC-2009-163, Ann Arbor, MI, September 20–24, 2009.

8. Shastry, R., Herman, D.A., Soulas, G.C., and Patterson, M.J., "End-of-test Performance and Wear Characterization of NASA's Evolutionary Xenon Thruster (NEXT) Long-Duration Test," 50th AIAA/ASME/SAE/ASEE Joint Propulsion Conference, AIAA-2014-3617, Cleveland, OH, July 28–30, 2014.

9. Shastry, R. and Soulas, G.C., "Post-test Inspection of NASA's Evolutionary Xenon Thruster Long-Duration Test Hardware: Discharge and Neutralizer Cathodes," 52nd AIAA/SAE/ASEE Joint Propulsion Conference, Salt Lake City, UT, July 25–27, 2016 (to be published).

10. Shastry, R. and Soulas, G.C., "Post-test Inspection of NASA's Evolutionary Xenon Thruster Long-Duration Test Hardware: Discharge Chamber," 52nd AIAA/SAE/ASEE Joint Propulsion Conference, Salt Lake City, UT, July 25–27, 2016 (to be published).

11. Herman, D.H., Soulas, G.C., and Patterson, M.J., "Status of the NEXT Ion Thruster Long-Duration Test After 10,100 h and 207 kg Demonstrated," 43rd AIAA/ASME/SAE/ASEE Joint Propulsion Conference and Exhibit, AIAA-2007-5272, Cincinnati, OH, July 8–11, 2007.

12. Diamant, K.D., et al., "Thrust Stand Characterization of the NASA NEXT Thruster," 46th AIAA/ASME/SAE/ASEE Joint Propulsion Conference & Exhibit, AIAA 2010-6701, Nashville, TN, July 25–28, 2010.

13. Sovey, J., Dever, J.A. and Power, J.L., "Retention of Sputtered Molybdenum on Ion Engine Discharge Chamber Surfaces," IEPC Paper 2001-086, 27th International Electric Propulsion Conference, Pasadena, CA, October 15–19, 2001.

14. Herman, D.A., Pinero, L.R., and Sovey, J.S., "NASA's Evolutionary Xenon Thruster (NEXT) Component Verification Testing," 44th AIAA/ASME/SAE/ASEE Joint Propulsion Conference and Exhibit, AIAA-2008-4812, Hartford, CT, July 21–23, 2008.

15. Patterson, M.J., et al., "Space Station Cathode Design, Performance, and Operating Specifications," 25th International Electric Propulsion Conference, IEPC-1997-170, Cleveland, OH, October 1997.

16. Kovaleski, S.D., et al., "A Review of Testing of Hollow Cathodes for The International Space Station Plasma Contactor," 27th International Electric Propulsion Conference, IEPC-2001-276, Pasadena, CA, October 15–19, 2001.

17. Hoskins, W.A., et al., "Development of a Prototype Model Ion Thruster for the NEXT System," 40th AIAA/ASME/SAE/ASEE Joint Propulsion Conference and Exhibit, AIAA-2004-4111, Fort Lauderdale, FL, July 11–14, 2004.

18. Polk, J.E., et al., "An Overview of the Results from an 8200 Hour Wear Test of the NSTAR Ion Thruster," 35th AIAA/ASME/SAE/ASEE Joint Propulsion Conference and Exhibit, AIAA-1999-2446, Los Angeles, CA, June 20–24, 1999.

19. Anderson, J.R., Sengupta, A., and Brophy, J.R., "Post-Test Analysis of the Deep Space One Spare Flight Thruster Ion Optics," 40th AIAA/ASME/SAE/ASEE Joint Propulsion Conference and Exhibit, AIAA-2004-3610, Fort Lauderdale, FL, July 11–14, 2004.

20. Sengupta, A., Brophy, J.R., and Goodfellow, K.D., "Status of the Extended Life Test of the Deep Space 1 Flight Spare Ion Engine After 30,352 Hours of Operation," 39th AIAA/ASME/SAE/ASEE Joint Propulsion Conference and Exhibit, AIAA-2003-4558, Huntsville, AL, July 20–23, 2003.

21. Sengupta, A, et al., "The 30,000-Hour Extended-Life Test of the Deep Space 1 Flight Spare Ion Thruster," NASA/TP 2004-213391, March 2005.

22. Pollard, J.E., et al., "Spatially-Resolved Beam Current and Charge-State Distributions for the NEXT Ion Engine," 46th AIAA/ASME/SAE/ASEE Joint Propulsion Conference & Exhibit, AIAA-2010-6779, Nashville, TN, July 25–28, 2010.

23. Doerner, R.P., Whyte, D.G., and Goebel, D.M., "Sputtering Yield Measurements during Low Energy Xenon Plasma Bombardment," *Journal of Applied Physics*, Vol. 93, No. 9, May 1, 2003, pp. 5816–5823.

24. Herman, D.A., "Review of the NASA's Evolutionary Xenon Thruster (NEXT) Long-Duration Test as of 632 kg of Propellant Throughput," 47th AIAA/ASME/SAE/ASEE Joint Propulsion Conference & Exhibit, AIAA-2011-5658, San Diego, CA, July 31-August 3, 2011.

25. Soulas, G.C., "The Impact of Back-Sputtered Carbon on the Accelerator Grid Wear Rates of the NEXT and NSTAR Ion Thrusters," 33rd International Electric Propulsion Conference, IEPC-2013-157, Washington, D.C., October 6–10, 2013.

26. Homa, J.M. and Wilbur, P.J., "Ion Beamlet Vectoring by Grid Translation," 16th AIAA/JSASS/DGLR International Electric Propulsion Conference, AIAA-1982-1895, New Orleans, LA, November 17–19, 1982.